Applied Surface Science 503 (2020) 144376

Contents lists available at ScienceDirect

Applied Surface Science

journal homepage: www.elsevier.com/locate/apsusc

Full Length Article

Thermal oxidation of amorphous Cu_xZr_{1-x} alloys: Role of composition-dependent thermodynamic stability

Yifei Xu[a], Yuanyuan Chen[a], Peter Schützendübe[b], Shengli Zhu[a], Yuan Huang[a], Zongqing Ma[a], Yongchang Liu[a], Zumin Wang[a,*]

[a] State Key Lab of Hydraulic Engineering Simulation and Safety, School of Materials Science and Engineering, Tianjin University, Tianjin 300350, China
[b] Max Planck Institute for Intelligent Systems, Heisenbergstrasse 3, D-70569 Stuttgart, Germany

ARTICLE INFO

Keywords:
Thermal oxidation
Amorphous alloys
Selective oxidation
Microstructure

ABSTRACT

The thermal oxidation of amorphous Cu–Zr alloys with different Cu:Zr ratios was studied by X-ray diffraction, Auger electron spectroscopy, and cross-sectional transmission electron microscopy. It was revealed that amorphous ZrO_2/Cu-enriched bilayers are formed on the amorphous Cu–Zr alloys at 200–250 °C by the selective oxidation of Zr atoms in the alloys. **Amorphous** Cu-enriched particles (diameter: **~10 nm**) are distributed randomly in the amorphous Cu-enriched sublayer of the am-$Cu_{33at.\%}Zr_{67at.\%}$ alloy, due to the sluggish atomic diffusion in the amorphous Cu-enriched layer. In contrast, **crystalline** Cu-enriched particles (diameter: **~20 nm**) are distributed densely in the amorphous Cu-enriched sublayer of the $Cu_{50at.\%}Zr_{50at.\%}$ alloy. The different states of the Cu-enriched particles in the amorphous Cu-enriched sublayer of the am-$Cu_{33at.\%}Zr_{67at.\%}$ and $Cu_{50at.\%}Zr_{50at.\%}$ alloys are ascribed to thermodynamic reasons. The oxidation rate of amorphous $Cu_{50at.\%}Zr_{50at.\%}$ alloy is faster than that of amorphous $Cu_{33at.\%}Zr_{67at.\%}$ alloy, since the crystalline nanoparticles in the Cu-enriched sublayer provide fast migration pathways for ions, whereas the thick amorphous Cu-enriched sublayer presents as a diffusion barrier in the case of amorphous $Cu_{33at.\%}Zr_{67at.\%}$ alloy.

1. Introduction

Oxidation occurs on the surfaces of alloys during service conditions, and this often contributes to the unwanted corrosion or degradation of the durability/reliability of the materials [1]. However, controlled oxidation, giving rise to surficial oxide formation, may assist the enhancement of the mechanical/functional properties of alloys, e.g., corrosion resistance, friction, catalytic activity, and electrical conductivity [2]. Therefore, comprehensive knowledge of the oxidation behaviours and mechanism of alloys is indispensable from the point of application.

The growth of oxide surficial layers depends strongly on the structures and compositions of the alloys. Amorphous alloys can form stable and homogenous oxide layers [3], in light of their more homogenous structures and the absence of defects compared to crystalline alloys. With regard to the effect of the composition of the amorphous alloys on the thermal oxidation, phase separation in the parent alloy can occur during oxidation of alloys composed of components with very different affinities to oxygen. This means that upon oxidation of an active–noble (A–N) alloy system, an AO_x/N-enriched double-layered structure is formed, induced by preferential oxidation of A. Such productive A–N alloys have raised intense interest for efficient synthesis (by oxidation treatment) and their ideal potential applications. For example, amorphous ZrO_2/Ni is used as a catalyst for the methanation reaction of H_2 and CO_2 [4].

Amorphous Cu–Zr alloy is a representative A–N amorphous alloy system because of the very different affinities to oxygen of Cu and Zr [5]. Cu–Zr-based amorphous alloys have been intensively studied due to their high glass-forming ability (GFA) [6,7], high thermal stability [8], and good mechanical properties, i.e., high strength and good ductility [9,10]. Previous studies on the thermal oxidation of the Cu–Zr amorphous system have shown good examples of favourable surface modification. For instance, the temperature coefficients of electrical resistivity of $Cu_{66}Zr_{34}$ amorphous ribbons can be adjusted by forming gradient-distributed surficial oxide phases with various thicknesses [11]. The combusted $Cu_{60}Zr_{40}$ amorphous ribbons performed good catalytic properties in the photocatalytic degradation of methylene blue and direct methanol fuel cells [12].

Isothermal and non-isothermal oxidation of amorphous Cu–Zr alloys at or above the supercooled liquid (SCL) region have been investigated systematically [13–16]. Studies on thermal oxidation behaviours of Cu–Zr alloys below the temperature range of SCL are lacking. In this

* Corresponding author.
E-mail address: z.wang@tju.edu.cn (Z. Wang).

https://doi.org/10.1016/j.apsusc.2019.144376
Received 18 July 2019; Received in revised form 3 October 2019; Accepted 10 October 2019
Available online 19 October 2019
0169-4332/

work, two amorphous Cu–Zr binary alloys with different compositions (amorphous $Cu_{33at.}Zr_{67at.\%}$ and $Cu_{50at.\%}Zr_{50at.\%}$) have been chosen as an A–N model system for the oxidation study due to the high GFA of Zr-rich amorphous Cu–Zr alloy (Cu content ≤ 50 at.%) [6,7]. The oxidation temperature range of 200–250 °C was chosen based on preliminary experiments and previous studies [15,17,18] to keep the amorphous Cu–Zr alloys in the amorphous state and eliminate the effect of crystallisation on the oxidation. The thermal oxidation of amorphous Cu–Zr alloys was investigated by a combined experimental approach, including X-ray diffraction (XRD), Auger electron spectroscopy (AES) depth profiling, and cross-sectional transmission electron microscopy (TEM). On this basis, the competition of the affinity to oxygen (thermodynamics factor) and the activity (kinetics factor) of the respective constituent elements during thermal oxidation of the amorphous alloys was revealed in depth.

2. Experimental

2.1. Specimen preparation and thermal oxidation

Thin coatings (thickness: ~2 μm, determined in a Veeco DekTak 8 profilometer) of am-$Cu_{33at.\%}Zr_{67at.\%}$ and am-$Cu_{50at.\%}Zr_{50at.\%}$ alloys were deposited onto Si (1 0 0) substrates by cosputtering pure Cu (purity 99.95 wt%) and pure Zr (purity 98.5 wt%) in a high-vacuum magnetron sputter system (base pressure ~5×10^{-7} Pa) [5]. Before the deposition, Si (1 0 0) wafers covered with amorphous Si_3N_4 (50 nm)/SiO_2 (50 nm) layers were sputter-cleaned by 105-eV Ar^+ ions. The chamber pressure was 0.5 Pa by introducing the Ar gas (purity 99.999 vol%, flow rate 18 sccm) during the deposition. The substrates were rotated with a speed of 10 rpm to improve the homogeneity of the specimens. The applied direct-current power was 100 W for the Zr target, and 20 and 40 W for the Cu target during the deposition of $Cu_{33at.\%}Zr_{67at.\%}$ and $Cu_{50at.\%}Zr_{50at.\%}$, respectively. The alloy compositions were determined by inductively coupled plasma optical emission spectroscopy (ICP-OES, Thermo iCAP 7400).

The as-deposited amorphous Cu–Zr alloys were then sealed in quartz tubes in a vacuum sealing system (MRVS-3002, Partulab Technology Co., Ltd). The tubes were first evacuated (base pressure ~1 Pa) and then backfilled with pure oxygen (purity 99.999 vol%) for three cycles. The oxygen partial pressures (p_{O_2}) in quartz tubes at room temperature were $p_{O_2} = 0.62$, $p_{O_2} = 0.59$, and $p_{O_2} = 0.56$ bar, corresponding to $p_{O_2} = 1$ bar at 200, 225, and 250 °C, respectively. The as-deposited amorphous Cu–Zr alloys were isothermally heated in a tube furnace (OTF-1200X, Hefei Kejing Materials Technology Co., Ltd.) at 200–250 °C for 1–10 h and quenched immediately in cold water.

2.2. X-ray diffraction

The as-deposited and oxidized Cu–Zr alloys were investigated by XRD on a Bruker D8 Advanced diffractometer equipped with a Cu X-ray anode (40 kV/40 mA, λ = 1.5418 Å). The XRD diffractograms were recorded in the diffraction angle (2θ) range of 10–65°, with a step size of 0.02° and a collection time of 0.15 s/step.

2.3. Auger electron spectroscopy sputter-depth profiling

The oxidized Cu–Zr alloys were investigated by AES sputter-depth profiling in a PHI 700Xi scanning Auger nanoprobe system (base pressure ~5×10^{-7} Pa), equipped with a field-emission electron gun operated at 5 kV. Sputter-depth profiling was performed by sputtering the specimens with 2-kV Ar^+ ions. The sputtering rate was calibrated by sputtering oxide layers with known thicknesses on the amorphous Cu–Zr samples (by TEM, see Section 2.5). The Cu *LMM*, Zr *MNN*, and O *KLL* Auger spectra were recorded after each successive ion-sputtering step. The concentration-depth profiles of the oxidic and metallic Zr were obtained by linear least-squares fitting of the corresponding differential AES spectra (MultiPak software, v.9.5.0.8). The quantifications of Zr in metallic (Zr^{met}) and oxidic (Zr^{ox}) states, as well as of Cu and O, were performed according to the procedure described in a previous work [19]. The relative sensitivity factors for metallic Cu and Zr were determined from the resolved peak-to-peak intensities of the am-$Cu_{33at.\%}Zr_{67at.\%}$ and am-$Cu_{50at.\%}Zr_{50at.\%}$ alloys (after sputtering the surficial oxides) and their known compositions (by ICP-OES). The relative sensitivity factors for oxidic Zr and O were determined from the resolved peak-to-peak intensity ratios, as recorded from thermally grown ZrO_2 on pure Zr. The determined relative sensitivity factors S (with respect to Zr^{met}) are: $S_{Zr^{met}} = 1.000$, $S_{Zr^{ox}} = 0.624$, $S_{Cu} = 0.408$, and $S_O = 1.336$.

2.4. Cross-sectional transmission electron microscopy specimen preparation

A focused ion beam (FIB) system (ZEISS Helios FIB/scanning-electron-microscopy crossbeam) was used to prepare cross-sectional TEM lamellae of the oxidized specimens. A Pt layer of 200 nm, followed by a second Pt layer of ~1 μm, was deposited on the area of interest by electron-beam evaporation and FIB deposition, respectively, to protect the lamella area from excessive ion beam damage during the FIB milling. The lamellae were then cut to a thickness of approximately 1.5 μm before being removed from the bulk specimen using an *in situ* lift-out technique. The lamellae were attached to the Cu grid and further thinned by 30-kV Ga^+ ions, with an ion beam current of 80–790 pA, and finally cleaned with 5-keV/14-pA and 2-keV/23-pA Ga^+ ions.

2.5. Transmission electron microscopy

The composition and structure of the oxide layers formed on the surface of the Cu–Zr alloys were examined by high-resolution TEM (HRTEM) using a FEI Tecnai G2 F30 S-TWIN electron microscope with a field emission gun operated at an acceleration voltage of 300 kV. The element distributions of specimens were investigated by energy dispersive X-ray spectroscopy (EDX) included in the microscope.

3. Results

3.1. Characterization of Cu–Zr alloys by XRD

The XRD patterns of the as-deposited and oxidized amorphous Cu–Zr alloys are shown in Fig. 1. Only a broad intensity hump maximum at approximately 36° in the 2θ range of 31–43° can be observed in the XRD pattern of as-deposited am-$Cu_{33at.\%}Zr_{67at.\%}$ alloy, as shown in Fig. 1a, thereby confirming its amorphous state. The amorphous state of the as-deposited alloy was further verified by the corresponding cross-sectional TEM observations (see Section 3.3). XRD patterns of the am-$Cu_{33at.\%}Zr_{67at.\%}$ alloy oxidized at temperatures of 200–250 °C for as much as 10 h further indicate that the thermal oxidation does not induce the crystallization of am-$Cu_{33at.\%}Zr_{67at.\%}$ alloy. Similarly, only a broad intensity hump maximum at approximately 38° in the 2θ range of 33–45° is observed in the XRD patterns of as-deposited and oxidized am-$Cu_{50at.\%}Zr_{50at.\%}$ alloys (Fig. 1b), also indicating the amorphous state of the as-deposited and oxidized am-$Cu_{50at.\%}Zr_{50at.\%}$ alloys.

3.2. AES measurements of the oxidized am-Cu–Zr alloys

The AES depth profiles of the am-$Cu_{33at.\%}Zr_{67at.\%}$ and am-$Cu_{50at.\%}Zr_{50at.\%}$ alloys oxidized at 200–250 °C for 1–10 h are shown in Figs. 2 and 3, respectively. It follows that the surficial regions of the thermally oxidized am-$Cu_{33at.\%}Zr_{67at.\%}$ and oxidized am-$Cu_{50at.\%}Zr_{50at.\%}$ alloys are composed of two sublayers: a ZrO_2 top layer and a Cu-enriched CuZr alloy layer underneath, as deduced by the AES element constitution as a function of the depth. Zr atoms react with O preferentially forming a ZrO_2 layer on top of the Cu–Zr alloy, and Cu atoms accumulate below the ZrO_2 to form a Cu-enriched layer. The

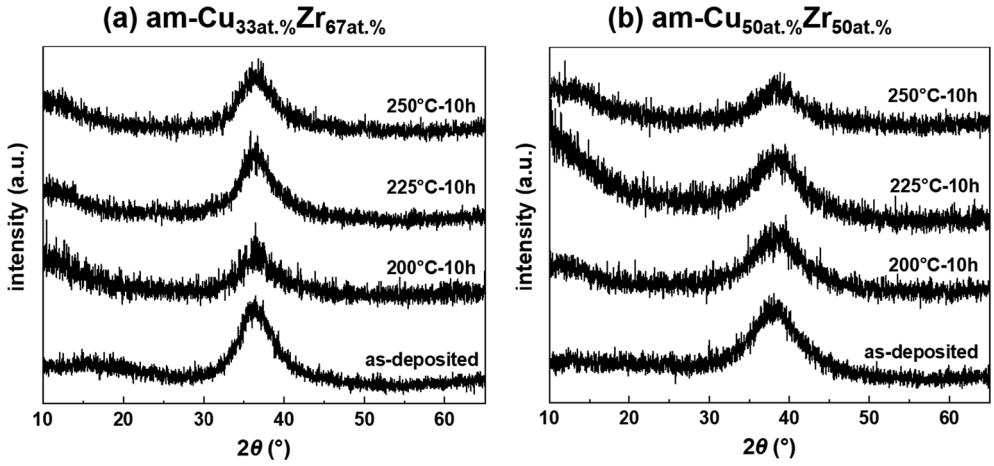

Fig. 1. XRD patterns of as-deposited and oxidized (a) am-$Cu_{33at.\%}Zr_{67at.\%}$ and (b) am-$Cu_{50at.\%}Zr_{50at.\%}$ alloys.

thicknesses of oxide layers (d_{ox}) and the Cu-enriched layer (d_{Curich}) and the concentration of dissolved oxygen (c_O) in the amorphous Cu–Zr alloys are listed in Table 1. The following conclusions can be drawn.

i. Passivation behaviour occurs for the am-$Cu_{33at.\%}Zr_{67at.\%}$ and am-$Cu_{50at.\%}Zr_{50at.\%}$ alloys. The ZrO_2 layers on the surface of the am-$Cu_{33at.\%}Zr_{67at.\%}$ alloy (thickness: 5.2–12.6 nm) and am-$Cu_{50at.\%}Zr_{50at.\%}$ alloy (thickness: 8.3–16.5 nm) grow very slowly at 200–250 °C due to the low oxygen diffusion in the passive amorphous ZrO_2 layers (3.2×10^{-8} m^2/s for ZrO_2 at 1000 °C [20]). By comparing the d_{ox} of 1, 4, and 10 h, the kinetics of oxidation of the am-$Cu_{33at.\%}Zr_{67at.\%}$ and am-$Cu_{50at.\%}Zr_{50at.\%}$ alloy at 200–250 °C

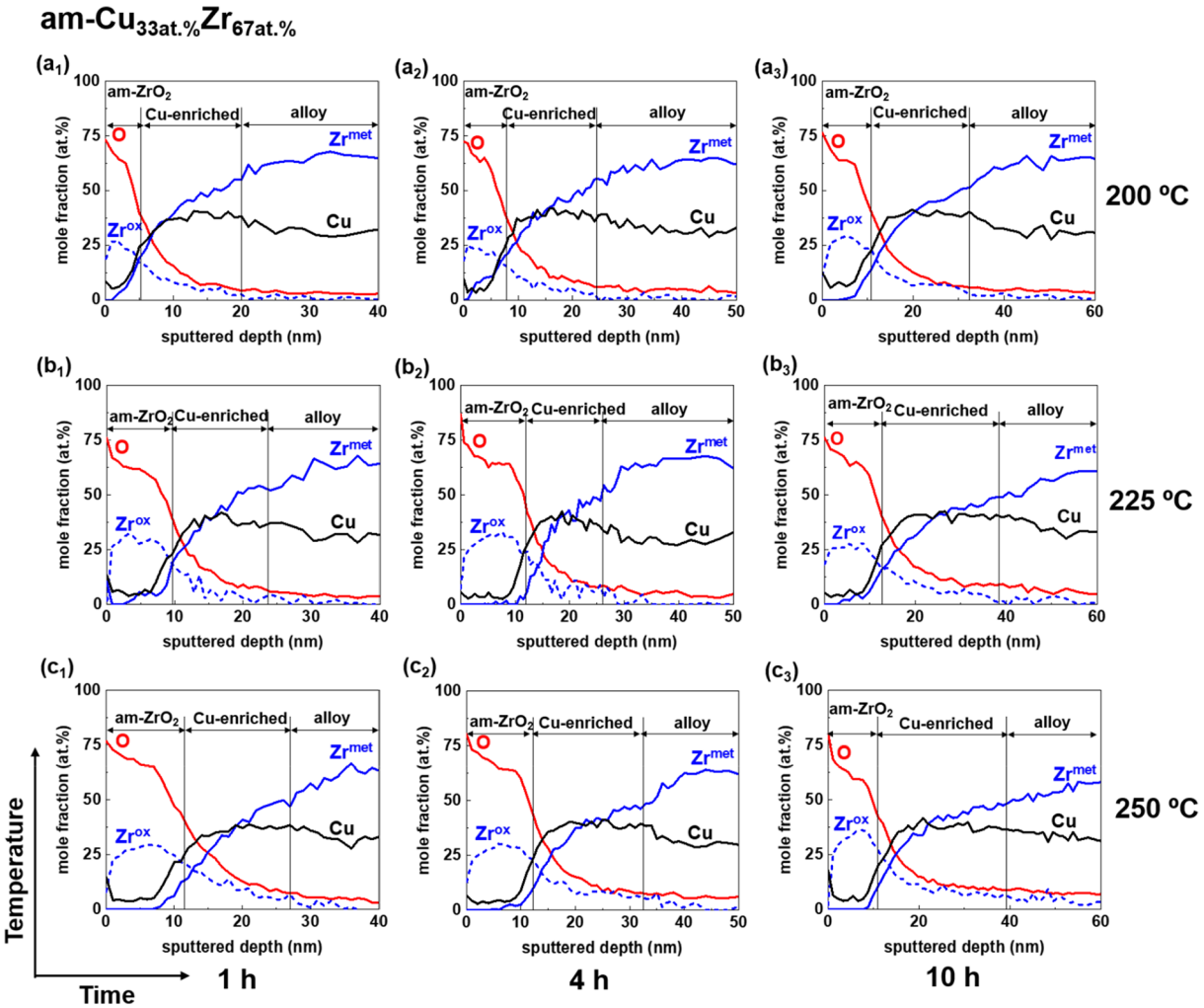

Fig. 2. AES depth-profiles of am-$Cu_{33at.\%}Zr_{67at.\%}$ alloy oxidized at (a_1) T = 200 °C and t = 1 h, (a_2) T = 200 °C and t = 4 h, (a_3) T = 200 °C and t = 10 h, (b_1) T = 225 °C and t = 1 h, (b_2) T = 225 °C and t = 4 h, (b_3) T = 225 °C and t = 10 h, (c_1) T = 250 °C and t = 1 h, (c_2) T = 250 °C and t = 4 h, and (c_3) T = 250 °C and t = 10 h.

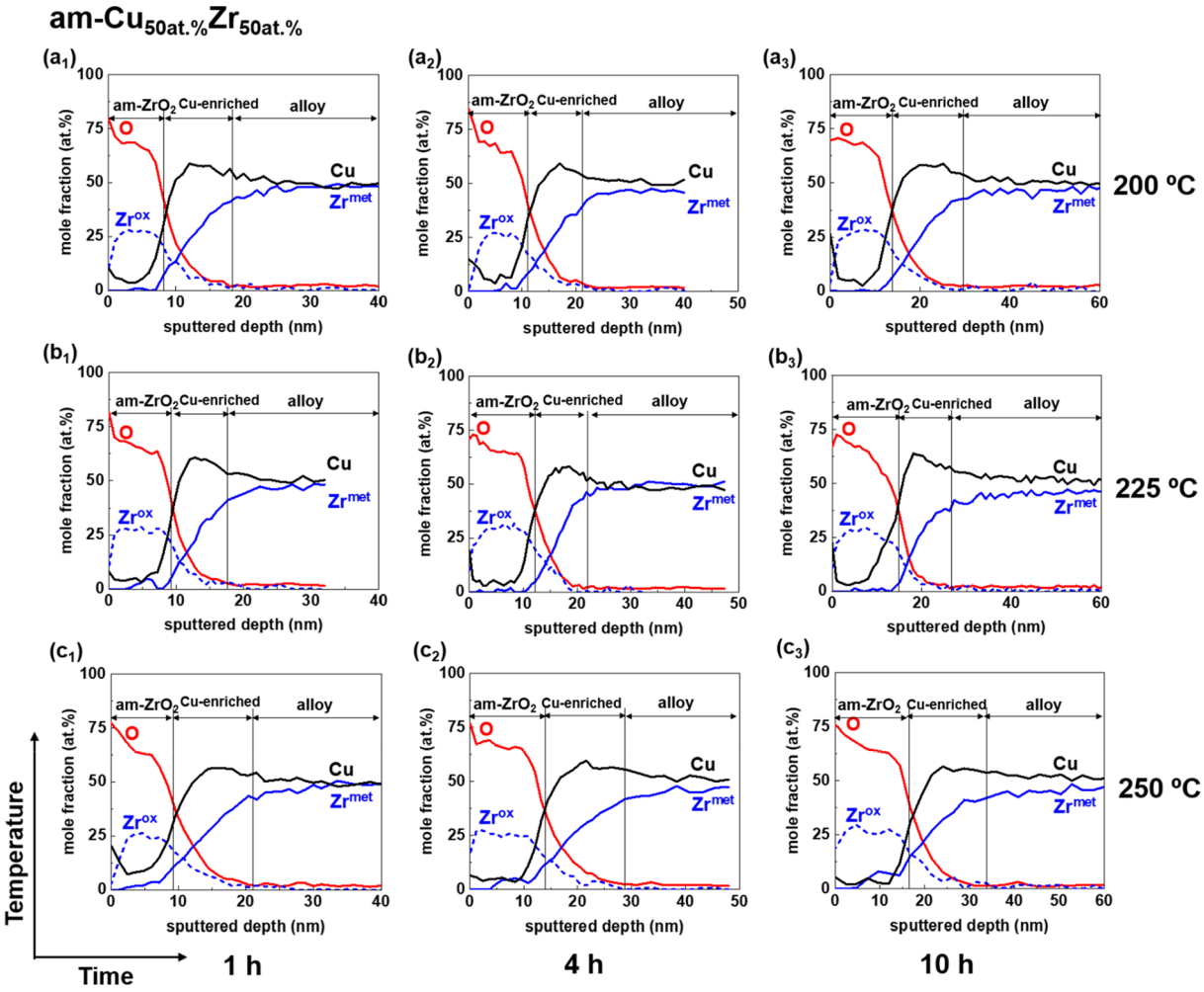

Fig. 3. AES depth-profiles of am-$Cu_{50at.\%}Zr_{50at.\%}$ alloy oxidized at (a_1) T = 200 °C and t = 1 h, (a_2) T = 200 °C and t = 4 h, (a_3) T = 200 °C and t = 10 h, (b_1) T = 225 °C and t = 1 h, (b_2) T = 225 °C and t = 4 h, (b_3) T = 225 °C and t = 10 h, (c_1) T = 250 °C and t = 1 h, (c_2) T = 250 °C and t = 4 h, and (c_3) T = 250 °C and t = 10 h.

Table 1
Thicknesses of oxide layers (d_{ox}) and Cu-enriched region (d_{Curich}) on the amorphous Cu-Zr alloys and concentration of dissolved oxygen in the amorphous Cu-Zr alloys (c_O).

Specimen	Time	d_{ox} ± 0.5 (nm)			d_{Curich} ± 0.5 (nm)			c_O ± 0.1 (at.%)		
		200 °C	225 °C	250 °C	200 °C	225 °C	250 °C	200 °C	225 °C	250 °C
am-$Cu_{33at.\%}Zr_{67at.\%}$	1 h	5.2	9.6	11.5	14.8	14.0	15.6	2.8	3.9	4.7
	4 h	7.9	11.9	12.3	16.5	14.1	20.1	3.3	4.5	5.5
	10 h	10.7	12.6	10.9	21.8	25.8	28.4	4.4	4.9	6.9
am-$Cu_{50at.\%}Zr_{50at.\%}$	1 h	8.3	9.2	9.2	10.1	8.4	11.8	2.4	2.1	2.0
	4 h	11.0	12.2	14.0	10.2	9.8	14.7	1.8	2.3	2.1
	10 h	13.8	14.9	16.5	15.7	11.8	17.3	2.0	2.6	1.8

practically obey a parabolic law, implying that the oxidations of both the two amorphous Cu–Zr alloys are controlled by ion diffusion.

ii. The oxidation of am-$Cu_{50at.\%}Zr_{50at.\%}$ alloy is obviously faster than that of the am-$Cu_{33at.\%}Zr_{67at.\%}$ alloy, as shown by comparing the d_{ox} formed on the two amorphous Cu–Zr alloys at the same oxidation condition (see Table 1 and Fig. 3).

iii. The Cu-enriched CuZr alloy layers (8.4–17.3 nm thick) formed in the am-$Cu_{50at.\%}Zr_{50at.\%}$ alloy are much thinner than those in the am-$Cu_{33at.\%}Zr_{67at.\%}$ alloy (14.0–28.4 nm thick).

iv. The Cu-enrichment is much more pronounced in am-$Cu_{50at.\%}Zr_{50at.\%}$ alloy. The highest Cu:Zr ratio of the Cu-enriched layer in the am-$Cu_{33at.\%}Zr_{67at.\%}$ alloy is approximately 1, whereas it is about 2.5 for that in the am-$Cu_{50at.\%}Zr_{50at.\%}$ alloy.

v. Approximately 2.8–6.9 (± 0.1) at.% oxygen dissolves in the am-$Cu_{33at.\%}Zr_{67at.\%}$ alloy at 200–250 °C, and the c_O increases slightly with increasing temperature. A obviously smaller amount of oxygen (1.8–2.6 at.%) dissolves in the am-$Cu_{50at.\%}Zr_{50at.\%}$ alloy than in the am-$Cu_{33at.\%}Zr_{67at.\%}$ alloy at 200–250 °C, irrespective of temperature. This is understandable, considering that O has high solubility in pure Zr, and practically no solubility in Cu [21,22]. Similar alloy-composition-dependent O solubility has also been observed in amorphous Al-Zr alloys [23].

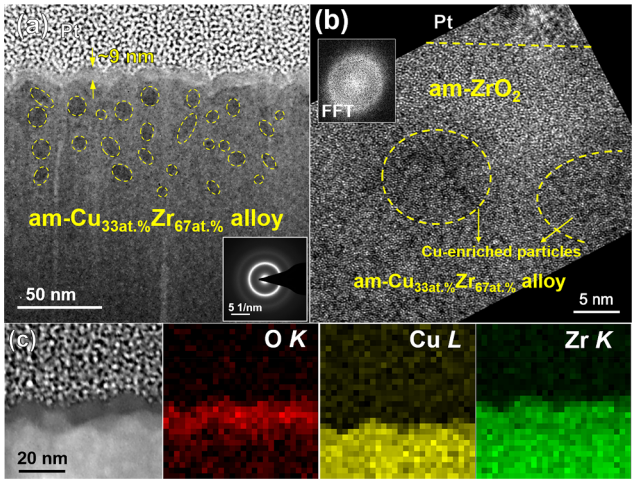

Fig. 4. (a) Cross-sectional TEM image of am-$Cu_{33at.\%}Zr_{67at.\%}$ alloy oxidized at 250 °C for 10 h, (b) HRTEM image and (c) EDX mapping of the surficial region on the oxidized am-$Cu_{33at.\%}Zr_{67at.\%}$ alloy.

3.3. Microstructure of the oxidized Cu–Zr alloys by cross-sectional HRTEM

The am-$Cu_{33at.\%}Zr_{67at.\%}$ and am-$Cu_{50at.\%}Zr_{50at.\%}$ alloys oxidized at 250 °C for 10 h were investigated by cross-sectional HRTEM. The selected-area electron diffraction (SAED) pattern (shown in the inset of Fig. 4a) shows that oxidized am-$Cu_{33at.\%}Zr_{67at.\%}$ alloy keeps the amorphous state. Fig. 4a shows that an am-ZrO_2 layer (thickness: ~9 nm, in accordance with the AES measurements) with a small roughness formed on top of the am-$Cu_{33at.\%}Zr_{67at.\%}$ alloy. The corresponding EDX mapping, as shown in Fig. 4c, also indicates that the surficial oxide layer was made of ZrO_2. Small spherical particles (diameter: ~10 nm) were distributed randomly in the Cu-enriched region (thickness: ~30 nm) between the am-ZrO_2 layer and the am-$Cu_{33at.\%}Zr_{67at.\%}$ alloy. Detailed fast Fourier transform (FFT) investigations in HRTEM images of those particles, as, for example, shown in the inset of Fig. 4b, indicate that the Cu-enriched particles are also amorphous.

Cross-sectional TEM investigation results of the oxidized am-$Cu_{50at.\%}Zr_{50at.\%}$ alloy are shown in Fig. 5. The SAED shown in the inset of Fig. 5a indicates the amorphous state of the am-$Cu_{50at.\%}Zr_{50at.\%}$ alloy after oxidation. A homogenous ZrO_2 layer with a thickness of ~15 nm formed on top of the am-$Cu_{50at.\%}Zr_{50at.\%}$ alloy, as observed in the cross-sectional TEM image in Fig. 5a. The corresponding EDX mapping, as shown in Fig. 5c, confirms that the surficial oxide layer was made of ZrO_2. The corresponding HRTEM observation shows that the ZrO_2 overlayer was also amorphous (Fig. 5b). A Cu-enriched layer, shown with dark contrast in Fig. 5a, formed underneath the amorphous ZrO_2 top layer. Some large nanoparticles (diameter: ~15–20 nm) were distributed densely in the Cu-enrich region (see Fig. 5a). In the corresponding HRTEM micrographs of the Cu-enriched particles (see Fig. 5b), clear lattice fringes are observed with lattice spacings of 3.064 and 3.30 Å (see also FFT in the inset), corresponding to the (1 0 3) lattice plane of the Cu_8Zr_3 phase [PDF#42-1186, Pnma(62)] and (0 2 2) lattice plane of the $Cu_{10}Zr_7$ phase [PDF#47-1028, C2ca(41)], respectively. The concentration ratios of Cu:Zr in Cu_8Zr_3 and $Cu_{10}Zr_7$ (2.2 and 1.5, respectively) are in accordance with the AES measurements (1.4–2.7, shown in Fig. 3). As a result, in contrast with the case of $Cu_{33at.\%}Zr_{67at.\%}$, the Cu-enriched layer between the top am-ZrO_2 layer and am-$Cu_{50at.\%}Zr_{50at.\%}$ alloy contains crystalline discrete/isolated Cu_8Zr_3 and $Cu_{10}Zr_7$ spherical particles.

4. Discussion

4.1. Microstructure of oxidized amorphous Cu–Zr alloys

Schematic illustrations of the microstructures of the thermally oxidized am-$Cu_{33at.\%}Zr_{67at.\%}$ and am-$Cu_{50at.\%}Zr_{50at.\%}$ alloys are shown in Fig. 6.

4.1.1. Formation of amorphous ZrO_2

Upon exposure of the amorphous Cu–Zr alloys to oxygen, Zr is preferentially oxidized (forming ZrO_2) due to its much higher affinity to oxygen than that of Cu. Although the crystalline (monoclinic) ZrO_2 is the most stable state for the zirconia [$(\Delta G_f(m\text{-}ZrO_2) < \Delta G_f(t\text{-}ZrO_2) < \Delta G_f(am\text{-}ZrO_2))$] [24], amorphous ZrO_2 with a thickness of several nanometres, rather than crystalline phases, forms at the initial oxidation of Zr-based alloys [5,19]. It is prevalent that the early overlapping of −O−M−O−M− chains with

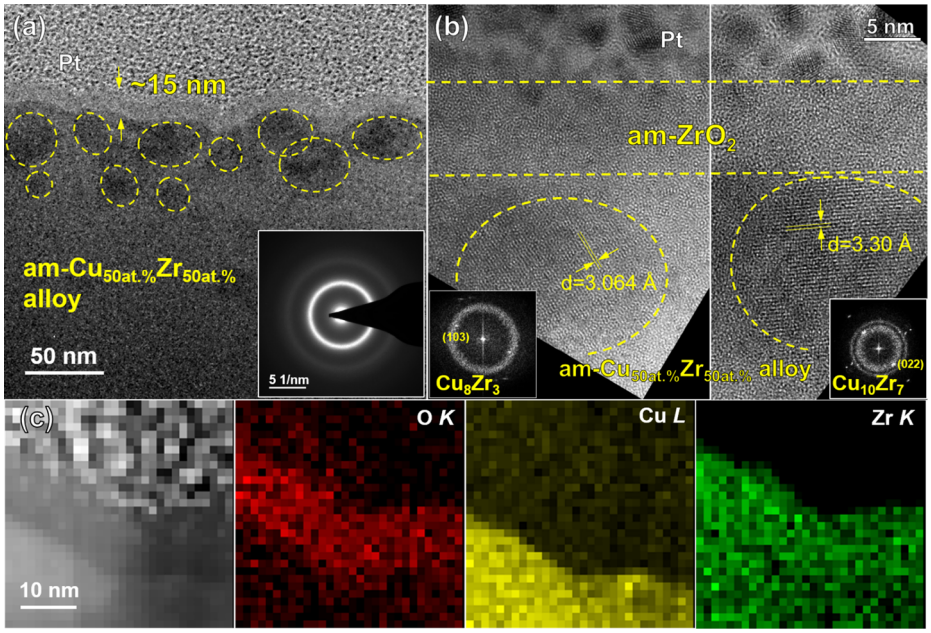

Fig. 5. (a) Cross-sectional TEM image of am-$Cu_{50\%}Zr_{50at.\%}$ alloy oxidized at 250 °C for 10 h, (b) HRTEM image and (c) EDX mapping of the surficial region on the oxidized am-$Cu_{50at.\%}Zr_{50at.\%}$ alloy.

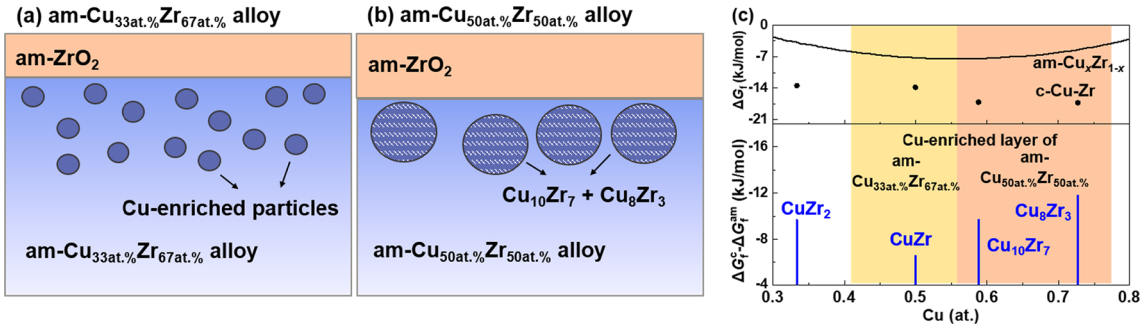

Fig. 6. Schematic illustration of microstructure of thermally oxidized (a) am-$Cu_{33at.\%}Zr_{67at.\%}$ and (b) am-$Cu_{50at.\%}Zr_{50at.\%}$ alloys, and (c) the calculated Gibbs energy of formation (ΔG_f) of am-Cu_xZr_{1-x} alloys (ΔG_f^{am}) [7], c-Cu-Zr alloys (ΔG_f^{c}) [30] at 250 °C (top inset) and the driving force ($\Delta G_f^{c} - \Delta G_f^{am}$) of the amorphous-crystalline transition of the Cu-enriched layer in the corresponding am Cu_xZr_{1-x} alloys (bottom inset).

each other (M refers to metal ions) subsequently promotes the emergence of an amorphous surficial oxide phase [19,25]. The formation of the new phase is basically related to the change of the Gibbs energy of formation, and it is significantly determined by the difference of strain and surface/interface energy between parent and product phases ($\Delta G_{barrier} = \Delta G_{strain} + \Delta\gamma + \Delta G_f$). The formation and growth of am-ZrO_2 are preferred due to negligible misfit-strain associated with amorphous ZrO_2 ($\Delta G_{strain} \approx 0$) and, further, to the lower surface and interface energies of am-ZrO_2 ($(\Delta\gamma(am\text{-}Zro_2) < \Delta\gamma(m\text{-}Zro_2))$. As a result, an amorphous ZrO_2 layer formed on top of the am-$Cu_{33at.\%}Zr_{67at.\%}$ and am-$Cu_{50at.\%}Zr_{50at.\%}$ alloys oxidized at 200–250 °C, as shown in Fig. 6a and b.

4.1.2. Formation of nanoparticles in the Cu-enriched region below am-ZrO_2

Due to the selective oxidation of Zr upon oxidation of am-$Cu_{33at.\%}Zr_{67at.\%}$ and $Cu_{50at.\%}Zr_{50at.\%}$ alloys, Cu accumulated beneath the amorphous ZrO_2 layer, forming a Cu-enriched region. Spherical nanoparticles were distributed in the Cu-enriched regions between the top am-ZrO_2 layer and the amorphous Cu–Zr substrates. Atomic diffusion is rather sluggish in the amorphous Cu–Zr alloys [17,26]. As a result, the accumulation of Cu in the amorphous Cu–Zr alloys as a result of the selective oxidation of Zr would occur in a rather localized and nonhomogeneous way, leading to the formation of Cu-enriched nanoparticles distributed in the Cu-enriched region.

4.1.3. Structure of nanoparticles in the Cu-enriched region

It is known [6,7,27,28] that the Gibbs energy of formation (ΔG_f) for amorphous Cu–Zr alloys decreases and then increases with increasing Zr fraction, and the lowest ΔG_f corresponds to a Zr fraction of 0.5, as shown in Fig. 6c. As reported by Lim et al. [13], oxidation induces the stabilization of the amorphous state of the subsurface region in the $Cu_{30}Zr_{70}$ metallic glass. The Zr-consumed subsurface region can keep an amorphous state, even at a temperature above the crystallization temperature (T_c) of the am-$Cu_{30}Zr_{70}$ substrate. In the case of the oxidized am-$Cu_{33at.\%}Zr_{67at.\%}$ alloy, the Cu-enriched layer beneath the surficial am-ZrO_2 layer has an average composition of Cu_xZr_{1-x} ($0.42 < x < 0.56$, see the AES results in Section 3.2), which is more stable than the am-$Cu_{33at.\%}Zr_{67at.\%}$ substrate (ΔG_f(Cu-rich) < ΔG_f(am-$Cu_{33at.\%}Zr_{67at.\%}$), see Fig. 6c). Furthermore, according to the Cu–Zr binary phase diagram [29], the crystalline phase closest to the composition of Cu_xZr_{1-x} ($0.42 < x < 0.56$) is CuZr, whose Gibbs energy of formation (ΔG_f) at 250 °C is (only) 6.8 kJ/mol lower than that of its amorphous counterpart. This is shown in Fig. 6c; for ΔG_f of am-$Cu_{50at.\%}Zr_{50at.\%}$ please refer to [7], and for ΔG_f of CuZr please refer to [30]. As a result, the Cu-enriched nanoparticles with an average composition of Cu_xZr_{1-x} ($x = 0.49 \pm 0.05$) tend to stay amorphous, as was observed (see Fig. 4), at a temperature lower than the glass transition temperature (T_g) of am-$Cu_{33at.\%}Zr_{67at.\%}$ alloy.

As for the am-$Cu_{50at.\%}Zr_{50at.\%}$ alloy, because of the enrichment of Cu under the ZrO_2 top layer, the formation Gibbs energy (ΔG_f) of the am-Cu_xZr_{1-x} alloy ($0.56 < x < 0.80$) is higher than that of the am-$Cu_{50at.\%}Zr_{50at.\%}$ alloy, as shown in Fig. 6c [28], which leads to a larger driving force for the crystallization of the Cu-enriched layer. The Cu–Zr crystalline phases corresponding to the Cu composition of 0.56–0.80 are Cu_8Zr_3 and $Cu_{10}Zr_7$, according to the binary phase diagram of the Cu–Zr system [29]. The Gibbs energies of formation (ΔG_f) of the Cu_8Zr_3 and $Cu_{10}Zr_7$ phases are 12.1 and 9.8 kJ/mol lower than those of their amorphous counterparts (ΔG_f of Cu_8Zr_3 and $Cu_{10}Zr_7$ at 250 °C [30]), large enough to drive the amorphous–crystalline transition. Indeed, observed by HRTEM in Fig. 6a, crystalline Cu_8Zr_3 and $Cu_{10}Zr_7$ nuclei grow to nanoparticles with a diameter of ~20 nm in the Cu-enriched sublayer.

4.1.4. Size and spatial distribution of nanoparticles in the Cu-enriched region

In the case of am-$Cu_{33at.\%}Zr_{67at.\%}$, the growth of amorphous nanoparticles is strongly obstructed because of the sluggish diffusion of Cu and Zr atoms in the Cu–Zr matrix. The enrichment of Cu during continuous selective oxidation of Zr from the Cu–Zr matrix can, therefore, only be realised by continuous formation of new, small nanoparticles (diameter: ≤10 nm) distributed broadly and randomly in the (wide) Cu-enrichment sublayer.

In contrast, during oxidation of am-$Cu_{50at.\%}Zr_{50at.\%}$ alloy, crystalline Cu–Zr alloy nanoparticles are formed. Compared with that in the am-$Cu_{50at.\%}Zr_{50at.\%}$ matrix, the local atomic diffusion is faster in those crystalline nanoparticles because of the fast diffusion pathway composed of energetically favourable interstitial sites [31]. As a result, the continued Cu-enrichment during oxidation of $Cu_{50at.\%}Zr_{50at.\%}$ alloys leads to the growth of crystalline $Cu_{10}Zr_7$ and Cu_8Zr_3 nanoparticles (diameter: ~20 nm), and the formation of new nanoparticles deep in the Cu-enriched region is hindered.

4.2. Oxidation kinetics of amorphous Cu–Zr alloys

It is indicated from the d_{ox} (see Table 1, Figs. 2 and 3) that the oxidation kinetics of am-$Cu_{33at.\%}Zr_{67at.\%}$ and am-$Cu_{50at.\%}Zr_{50at.\%}$ alloys both obey a parabolic law. Therefore, the outward diffusion of metallic ions and/or the inward diffusion of oxygen ions are the controlling step of the thermal oxidation of am-$Cu_{33at.\%}Zr_{67at.\%}$ and am-$Cu_{50at.\%}Zr_{50at.\%}$ alloys at 200–250 °C. Kai et al. [15] found that the oxidation kinetics of the $Cu_{50}Zr_{50}$ bulk metallic glass generally followed a parabolic-rate law at 350–425 °C. Other studies [32–38] have also shown the parabolic kinetics and, thus, the ion diffusion controlled oxidation of Cu–Zr-based amorphous alloys.

The amorphous Cu-enriched layer in the thermally oxidized am-$Cu_{33at.\%}Zr_{67at.\%}$ alloy induced by the preferential oxidation of Zr, is 14.0–28.4 nm thick and 1.5–2 times that of the ZrO_2 layers above, because of the growth of the amorphous nanoparticles (see Section 4.1.4).

The energy barrier of oxygen inward diffusion and metallic-ion outward diffusion in the thick amorphous Cu-enriched layer of the am-$Cu_{33at.\%}Zr_{67at.\%}$ alloy is substantially elevated as a result of the absence of the diffusion pathways made up of periodic arranged interstitial sites. The oxidation of am-$Cu_{33at.\%}Zr_{67at.\%}$ alloy is restricted with the growth of the amorphous Cu-enriched layer.

However, the subsurface layer of am-$Cu_{50at.\%}Zr_{50at.\%}$ alloy crystallizes to Cu_8Zr_3 and $Cu_{10}Zr_7$ phases as result of the Cu enrichment during thermal oxidation (see Fig. 5a and Section 4.1). The crystalline Cu-enriched particles (Cu_8Zr_3 and $Cu_{10}Zr_7$), as well as their interfaces with the amorphous alloy matrix, can provide pathways for diffusion of oxygen and metallic ions [31]. Although the diffusion rate of ions in the am-$Cu_{50at.\%}Zr_{50at.\%}$ alloy is lower than that in am-$Cu_{33at.\%}Zr_{67at.\%}$ alloy, the oxidation of the am-$Cu_{50at.\%}Zr_{50at.\%}$ alloy is accelerated by the presence of a high density of crystalline Cu-enriched particles compared with the $Cu_{33at.\%}Zr_{67at.\%}$ alloy, whose oxidation is hindered by the thick amorphous Cu-enriched diffusion barrier.

5. Conclusions

- Amorphous ZrO_2 layers (thickness: 5.2–16.5 nm) were formed at 200–250 °C on top of am-$Cu_{33at.\%}Zr_{67at.\%}$ and am-$Cu_{50at.\%}Zr_{50at.\%}$ alloys by the selective oxidation of Zr because of the lower strain energy and interface energy of the amorphous oxide phase.
- Due to the sluggish atomic diffusion in the amorphous Cu–Zr alloys, the Cu accumulation underneath the top ZrO_2 as a result of the selective oxidation of Zr occurred in a rather localised and non-homogeneous way, leading to the formation of Cu-enriched nanoparticles.
- The Cu-enriched spherical nanoparticles in the Cu-enriched region of $Cu_{33at.\%}Zr_{67at.\%}$ and $Cu_{50at.\%}Zr_{50at.\%}$ alloys were amorphous and crystalline, respectively, due to the different driving force for the corresponding crystallisation of the amorphous Cu-enriched layer.
- Small amorphous Cu-enriched nanoparticles (diameter: ~10 nm), whose growth was restricted by the sluggish atomic diffusion in the amorphous Cu-enriched region, distributed in a dispersed manner in the Cu-enriched region of am-$Cu_{33at.\%}Zr_{67at.\%}$ alloy with the thickening of Cu-enrichment region. In contrast, large Cu_8Zr_3 and $Cu_{10}Zr_7$ crystalline nanoparticles (diameter: ~20 nm), growing faster due to the faster ion diffusion in the crystalline nanoparticles, were distributed densely in the Cu-enriched region of the am-$Cu_{50at.\%}Zr_{50at.\%}$ alloy.
- The oxidation rate of the am-$Cu_{33at.\%}Zr_{67at.\%}$ alloy was lower than that of the am-$Cu_{50at.\%}Zr_{50at.\%}$ alloy because of the thick amorphous Cu-enriched layer as an ion diffusion barrier and the lack of crystalline Cu_8Zr_3 and $Cu_{10}Zr_7$ particles providing ion migration pathways, i.e., ordered interstitial sites and defects.

Acknowledgements

The authors are grateful to Dr. Lars P.H. Jeurgens for helpful discussion. This work is supported financially by the National Natural Science Foundation of China (No. 51571148), the National Key Research and Development Program of China (No. 2017YFE0302600 and No. 2017YFB0701801), and the Thousand Talents Program for Distinguished Young Scholars of China.

References

[1] H. Over, A.P. Seitsonen, Oxidation of metal surfaces, Science 297 (2002) 2003.
[2] N. Birks, G.H. Meier, F.S. Pettit, Introduction to the High Temperature Oxidation of Metals, Cambridge University Press, Cambridge, 2006.
[3] K. Weller, Z.M. Wang, L.P.H. Jeurgens, E.J. Mittemeijer, Thermodynamics controls amorphous oxide formation: exclusive formation of a stoichiometric amorphous $(Al_{0.33}Zr_{0.67})O_{1.83}$ phase upon thermal oxidation of Al–Zr, Acta Mater. 94 (2015) 134–142.
[4] M. Yamasaki, H. Habazaki, K. Asami, K. Izumiya, K. Hashimoto, Effect of tetragonal ZrO_2 on the catalytic activity of Ni/ZrO_2 catalyst prepared from amorphous Ni-Zr alloys, Catal. Commun. 7 (2006) 24–28.
[5] Y. Xu, X. Liu, L. Gu, J. Wang, P. Schützendübe, Y. Huang, Y. Liu, Z. Wang, Natural oxidation of amorphous Cu_xZr_{1x} alloys, Appl. Surf. Sci. 457 (2018) 396–402.
[6] G. Shao, Prediction of amorphous phase stability in metallic alloys, J. Appl. Phys. 88 (2000) 4443–4445.
[7] N. Saunders, A.P. Miodownik, Thermodynamic aspects of amorphous phase formation, J. Mater. Res. 1 (1985) 38–46.
[8] M. Apreutesei, P. Steyer, A. Billard, L. Joly-Pottuz, C. Esnouf, Zr–Cu thin film metallic glasses: an assessment of the thermal stability and phases' transformation mechanisms, J. Alloy. Compd. 619 (2015) 284–292.
[9] A. Inoue, A. Takeuchi, Recent progress in bulk glassy alloys, Mater. Trans. 43 (2002) 1892–1906.
[10] A. Inoue, W. Zhang, T. Zhang, K. Kurosaka, Thermal and mechanical properties of Cu-based Cu-Zr-Ti bulk glassy alloys, Mater. Trans. 42 (2001) 1149–1151.
[11] B. Liu, C. Han, F. Ye, Adjustment of temperature coefficient of electrical resistivity in $Cu_{66}Zr_{34}$ metallic glass through surface oxidation induced phase decomposition, Corros. Sci. 125 (2017) 166–174.
[12] X. Li, J. Wu, Y. Pan, Preparation of nanostructured Cu/Zr metal mixed oxides via self-sustained oxidation of a CuZr binary amorphous alloy, J. Mater. Sci. Technol. 35 (2019) 1601–1606.
[13] K.R. Lim, J.M. Park, S.H. Park, M.Y. Na, K.C. Kim, W.T. Kim, D.H. Kim, Oxidation induced amorphous stabilization of the subsurface region in Zr-Cu metallic glass, Appl Phys Lett 104 (2014).
[14] K.R. Lim, W.T. Kim, E.-S. Lee, S.S. Jee, S.Y. Kim, D.H. Kim, A. Gebert, J. Eckert, Oxidation resistance of the supercooled liquid in $Cu_{50}Zr_{50}$ and $Cu_{46}Zr_{46}Al_8$ metallic glasses, J. Mater. Res. 27 (2012) 1178–1186.
[15] W. Kai, W.S. Chen, Y.H. Wu, P.C. Lin, C.P. Chuang, P.K. Liaw, Air-oxidation of a $Cu_{50}Zr_{50}$ binary amorphous ribbon at 350–425 °c, J. Alloy. Compd. 536 (2012) S103–S108.
[16] U. Koester, L. Jastrow, Oxidation of Zr-based metallic glasses and nanocrystalline alloys, Mater. Sci. Eng. a-Struct. Mater. Prop. Microstruct. Process. 449 (2007) 57–62.
[17] M. Kluge, H.R. Schober, Diffusion and jump-length distribution in liquid and amorphous $Cu_{33}Zr_{67}$, Phys. Rev. B 70 (2004) 224209.
[18] W.H. Wang, J.J. Lewandowski, A.L. Greer, Understanding the glass-forming ability of Cu50Zr50 alloys in terms of a metastable eutectic, J. Mater. Res. 20 (2011) 2307–2313.
[19] K. Weller, L.P.H. Jeurgens, Z. Wang, E.J. Mittemeijer, Thermal oxidation of amorphous $Al_{0.44}Zr_{0.56}$ alloys, Acta Mater. 87 (2015) 187–200.
[20] F.J. Keneshea, D.L. Douglass, The diffusion of oxygen in Zirconia as a function of oxygen pressure, Oxid. Met. 3 (1971) 1–14.
[21] J.P. Abriata, J. Garcés, R. Versaci, The O−Zr (Oxygen-Zirconium) system, Bull. Alloy Phase Diagrams 7 (1986) 116–124.
[22] M.L. Narula, V.B. Tare, W.L. Worrell, Diffusivity and solubility of oxygen in solid copper using potentiostatic and potentiometric techniques, Metall. Trans. B 14 (1983) 673–677.
[23] K. Weller, Z.M. Wang, L.P.H. Jeurgens, E.J. Mittemeijer, Oxidation kinetics of amorphous Al_xZr_{1-x} alloys, Acta Mater. 103 (2016) 311–321.
[24] M.W. Chase Jr., NIST-JANAF thermochemical tables, 1998.
[25] L. Luo, Y. Kang, J.C. Yang, G. Zhou, Effect of oxygen gas pressure on orientations of Cu_2O nuclei during the initial oxidation of Cu(100), (110) and (111), Surf. Sci. 606 (2012) 1790–1797.
[26] Y. Zhang, C.Z. Wang, M.I. Mendelev, F. Zhang, M.J. Kramer, K.M. Ho, Diffusion in a Cu-Zr metallic glass studied by microsecond-scale molecular dynamics simulations, Phys. Rev. B 91 (2015) 180201.
[27] W.F. Wu, Y. Li, Bulk metallic glass formation near intermetallic composition through liquid quenching, Appl. Phys. Lett. 95 (2009) 011906.
[28] Y.C.K.O.J. Kwon, K.B. Kim, Y.K. Lee, E. Fleury, Formation of amorphous phase in the binary Cu-Zr, Met. Mater. Int. 12 (2006) 207–212.
[29] D. Arias, J.P. Abriata, Cu-Zr (Copper-Zirconium), J. Phase Equilibria 11 (1990) 452–459.
[30] S.H. Zhou, R.E. Napolitano, Phase stability for the Cu–Zr system: first-principles, experiments and solution-based modeling, Acta Mater. 58 (2010) 2186–2196.
[31] B. Lee, B. Lee, A comparative study on hydrogen diffusion in amorphous and crystalline metals using a molecular dynamics simulation, Metallurgical Mater. Trans. A 45 (2014) 2906–2915.
[32] W. Kai, P.C. Lin, W.S. Chen, C.P. Chuang, P.K. Liaw, H.H. Huang, H.H. Hsieh, Air-oxidation of a $Zr_{50}Cu_{43}Al_7$ bulk metallic glass at 400–500°C, Corros. Sci. 64 (2012) 98–104.
[33] J.L. Zhang, W.H. Cao, C.H. Shek, Silver mushroom induced by oxidation in $Cu_{42}Zr_{42}Al_8Ag_8$ metallic glasses, J. Alloy. Compd. 509 (Supplement 1) (2011) S219–S222.
[34] W. Kai, I.F. Ren, P.C. Kao, R.F. Wang, C.P. Chuang, M.W. Freels, P.K. Liaw, Air-oxidation of a $Cu_{45}Zr_{45}Al_5Ag_5$ bulk metallic glass, Adv. Eng. Mater. 11 (2009) 380–386.
[35] C.Y. Tam, C.H. Shek, W.H. Wang, Oxidation behaviour of a Cu-Zr-Al bulk metallic glass, Rev. Adv. Mater. Sci. 18 (2008) 107–111.
[36] M. Zhang, D. Yao, X. Wang, L. Deng, Air oxidation of a $Zr_{55}Cu_{30}Al_{10}Ni_5$ bulk metallic glass at its super cooled liquid state, Corros. Sci. 82 (2014) 410–419.
[37] B. Wang, D.Y. Huang, N. Prud'homme, Z. Chen, F. Jomard, T. Zhang, V. Ji, Diffusion mechanism of Zr-based metallic glass during oxidation under dry air, Intermetallics 28 (2012) 102–107.
[38] X.P. Nie, X.H. Yang, L.Y. Chen, K.B. Yeap, K.Y. Zeng, D. Li, J.S. Pan, X.D. Wang, Q.P. Cao, S.Q. Ding, J.Z. Jiang, The effect of oxidation on the corrosion resistance and mechanical properties of a Zr-based metallic glass, Corros. Sci. 53 (2011) 3557–3565.